DOI: 10.13009/EUCASS2022-4541
9TH EUROPEAN CONFERENCE FOR AERONAUTICS AND SPACE SCIENCES (EUCASS)

Loads prediction at early stage of water landing on amphibious aircraft with a V-shaped hull

Yujin Lu[1,2], Alessandro Del Buono[2], Tianhang Xiao[1], Alessandro Iafrati[2], Shuanghou Deng[1]
[1] *Nanjing University of Aeronautics and Astronautics*
Yudao Street 29, Nanjing, 210016, People's Republic of China
[2] *National Research Council–Institute of Marine Engineering (CNR-INM)*
Via di Vallerano 139, Rome, 00128, Italy

Abstract
The water landing motion of an amphibious aircraft is a complicated problem that can lead to uncomfortable riding situation and structural damage. The problem herein is investigated by solving unsteady incompressible Reynolds-averaged Navier-Stokes equations with a standard k-ω turbulence closure model. The theoretical solutions established by the momentum theory are also employed. In order to validate the relationship between initial vertical velocity and peak value of vertical acceleration, free fall test case of 2D symmetric wedge is presented first. Other corresponding parameters, such as time, penetration depth, vertical velocity, are also evaluated. Subsequently, the quantitative relations are investigated for amphibious aircraft. The results show that a linear dependence of the maximal acceleration from the square of initial vertical velocity can be derived for wedge and seaplane. Moreover, the ratio between the corresponding vertical velocity and the initial vertical velocity tends to a constant threshold value, 5/6, when increasing initial vertical velocity in all three cases.

1. Introduction

Amphibious aircraft is a special flight vehicle that can take off and land on both water and conventional runways on airports [1]. Its functions can be essentially divided into two categories. The first one is basically for general aviation, i.e. firefighting, sea sightseeing tourism, etc. On the other hand, potential military, concerning marine patrol, anti-submarine, rescue and so on, can be considered as the second application. On the whole, due to its inherent operational situations, the most circumstances that the aircraft may face are open water field, leading to the water impacting load as the primary load conditions, which involves sorts of complicated physical and hydrodynamic phenomena [2].
Moreover, the term of peak vertical acceleration is more significant, which not only causes mental problems for the crews but also it can lead to structural damages for the fuselage once it strikes the water [3], deserving more attentions amid the load characteristics about an amphibious aircraft landing on water. It is well known that less time to reach the peak value for larger initial vertical velocity, however, it will be beneficial and convenient for experimental test or simulation if there exists some theoretical or empirical formula to guide on the water entry phenomenon, especially for the complicated model like an amphibious aircraft.
Similar to the water landing scenarios of amphibian aircraft, ditching events of conventional aircrafts share the same fluid dynamics phenomena. it is usually distinguished in four phases: approach, impact, landing, and flotation [4]. The impact phase is the most important one in terms of complex fluid-structure interaction. Von Karman [5] first proposed an analytical estimation method based on a wedge-shaped water impact and introduced the method to settle the impact loads on seaplanes. Subsequently, a number of researches related to water impact have been carried out based on theoretical, computational or experimental approaches [6]-[13]. It has been shown that, in the case of free-fall, the structure experiences a rapid change of vertical acceleration and velocity, which is similar to what happens in the impact phase of the water landing[14]. Several studies have focused the attention on the relationship between the maximum acceleration and initial parameters on free-fall water entry. Among these studies, Gong et al. [15] simulated a series of cases with various initial entering velocity of the wedge based on Smoothed Particle Hydrodynamics (SPH) model, and relations for the maximum force on the wedge and the corresponding time in terms of the initial entering velocity of the wedge have been directly expressed by fitting formulas with Froude number greater than 2. In the work of Abraham et al [16], the drag-coefficient of a sphere impacting the water surface was found to be independent of some investigated quantities, like the sphere velocity, surface tension, flow regime (laminar or turbulent) and Reynolds number. Hence, algebraic expressions of the drag coefficient versus the dimensionless depth have been established by two fitted polynomials. Effects of parametric variation, such as impact velocity, radius, and mass of the sphere on the impact force and the acceleration, have also been analysed by Yu et al [17]. The peak value of the non-dimensional impact force has been found to be independent of the velocity and the radius, whereas it depends on the mass of sphere. In parallel, simplified expressions for the maximal force and the acceleration have been obtained through fitting the

DOI: 10.13009/EUCASS2022-4541

relations between the peak value of the non-dimensional force and the non-dimensional mass. However, it has to be noted that only fitting functions of force and acceleration were discussed in the previous studies, whereas the detailed theoretical basis with related relationships have not been derived yet.
The present study is dedicated to numerical simulations of a two-dimensional symmetric wedge in free fall water entry in order to investigate and build up parametric relations, based on the transformation of conservation of momentum theory, that can provide the maximal vertical acceleration and the corresponding vertical velocity, penetration depth and time. Particular attention is paid at the effects of horizontal velocity. The relations are then used to predict the load acting on amphibious aircraft during the water landing. The present work outlines as follows. Section 2 presents the methodology for the theoretical and numerical approaches, and describes the models and computational setup; the main results are reported and discussed in Sec. 3; final conclusions are drawn in Sec. 4.

2. Methodology and Computational Setup

2.1 Von Karman's theoretical method and transformation

Pioneer research in water-entry problem has been conducted by von Karman [5], based on momentum theorem and the added mass for the force prediction as the V-shaped body penetrates the water surface. The theorem of momentum equation for predicting hydrodynamic load of water entry can be concluded during the impacting, that is,

$$M\upsilon_0 = (M + m_{\text{added}}) \cdot \upsilon(t) \tag{1}$$

where M is the mass of the wedge per unit length, υ_0 is the initial vertical velocity before the impact, $\upsilon(t)$ is the instantaneous velocity during impacting and m_{added}, namely added mass briefly computed by $m_{\text{added}} = (\pi\rho r^2(t))/2$ (see Figure 1), using the flat-plate approximation of the added mass. It is assumed the mass of a half disk of water of radius $r(t)$ is moving with the wedge [18], ignoring the effect of water pile-up herein. By this way, the velocity of the body can be formulated by:

$$\upsilon(t) = \frac{M\upsilon_0}{M + m_{\text{added}}} = \frac{M\upsilon_0}{M + \dfrac{\pi\rho z^2(t)}{2\tan^2(\beta)}} = \frac{2M\tan^2(\beta)\upsilon_0}{2M\tan^2(\beta) + \pi\rho z^2(t)} \tag{2}$$

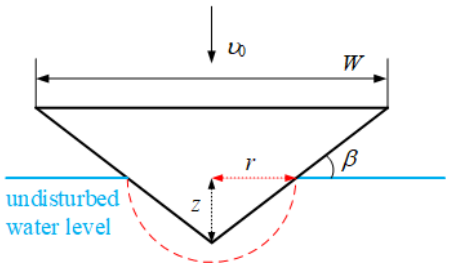

Figure 1: Von Karman's momentum approach.

By differentiating Eq. (2), it is possible to analytically calculate the instantaneous acceleration as followed [19]:

$$a(t) = \frac{\pi\rho z(t)}{M\upsilon_0 \tan^2(\beta)} \cdot \upsilon^3(t) \tag{3}$$

The impact acceleration reaches its peak as:

$$a^* = \upsilon_0^2 \left(\frac{5}{6}\right)^3 \frac{1}{\tan(\beta)} \sqrt{\frac{2\pi\rho}{5M}} \tag{4}$$

when the corresponding penetration depth and velocity are:

DOI: 10.13009/EUCASS2022-4541

$$\begin{cases} z^* = \sqrt{\dfrac{2M}{5\pi\rho}}\tan(\beta) \\ \upsilon^* = \dfrac{5}{6}\upsilon_0 \end{cases} \tag{5}$$

It should be noticed that we define the positive direction of acceleration upwards, while the velocity and penetration depth are positive downwards. Moreover, according to the work of [19] and [20], the corresponding time t^* can be expressed as:

$$t^* = \frac{1}{\upsilon_0}\frac{16}{15}\sqrt{\frac{2M}{5\pi\rho}}\tan(\beta) \tag{6}$$

Note that the superscript * indicates the values the different quantities take when the acceleration reaches its peak. It is interesting to notice that a^*, $\upsilon^*$and t^*, are proportional to υ_0^2, υ_0 and υ_0^{-1} respectively, implying that the initial vertical velocity governs those parameters, except z^*.

2.2 Numerical method

In the present study the unsteady incompressible Reynolds-averaged Navier-Stokes equations with a standard *k-ω* two-equation turbulence model are solved by the finite volume method. The Semi-Implicit Pressure Linked Equations (SIMPLE) algorithm is employed to achieve an implicit coupling between pressure and velocity, and the gradient is reconstructed with the Green-Gauss Node Based method. The modified High Resolution Interface Capturing (HRIC) scheme is adopted to volume fraction discretization. The convection terms, as well as diffusion terms, are turned into algebraic parameters using second-order upwind and second-order central methods, respectively. The unsteady terms are discretized in the time domain by applying a second-order implicit scheme.
Volume of fluid (VOF) scheme, first proposed by Hirt and Nichols [21], is used in the present computational scheme to capture the water-air interface by introducing a variable called the volume fraction of the water in the computational cell, shown by α_w, which varies between 0 (air) and 1 (water), defined as:

$$\alpha_w = V_w / V\,, \tag{7}$$

where V_w is the volume of water in the cell and V is the volume of the cell. The volume fractions of two phases in a cell must sum up to one:

$$\alpha_w + \alpha_a = 1\,. \tag{8}$$

The effective value φ_m of any physical properties, such as density, viscosity, etc., of the mixture of water and air in the transport equations is determined by:

$$\varphi_m = \varphi_w\alpha_w + \varphi_a(1-\alpha_w)\,. \tag{9}$$

To accurately capture the dynamic behavior as well as the load characteristics of water landing process, the motion of the body in response to the fluid forces and moments at the surface is determined using a six degree-of-freedom (6DOF) model. The 6DOF model solves the equations for the rotation and translation of the center of mass of the object. The equation for the translation in the global inertial coordinate system is formulated as:

$$M\cdot\frac{d\boldsymbol{v}}{dt} = \boldsymbol{F}\,, \tag{10}$$

and the rotation of the object is solved in the body local coordinate system by:

$$\boldsymbol{L}\frac{d\boldsymbol{\omega}}{dt} + \boldsymbol{\omega}\times\boldsymbol{L}\boldsymbol{\omega} = \boldsymbol{M}\,. \tag{11}$$

DOI: 10.13009/EUCASS2022-4541

where $\boldsymbol{L}$ is the tensor of the moments of inertia, $\boldsymbol{M}$ is the resultant moment acting on the object and $\boldsymbol{\omega}$ is the angular velocity of the object.
Subsequently, a dynamic mesh strategy [22], which moves the entire fluid mesh rigidly along with the object at each time step according to the solution of the six-degree-freedom model, is employed to deal with the relative motion between the fluid and the rigid body with one single grid domain. As neither mesh distortion nor mesh reconstruction occurs, the high quality of the initial mesh remains unchanged during the whole simulation, and thus, the solution accuracy of both flow field and water-air interface capture is not degraded for such unsteady problems with large relative motion. It should be mentioned that the water surface level is kept stationary regardless of the translation or rotation of the mesh. To achieve this goal, the function of α_w needs to be implemented on the boundary condition where the water volume fraction of each grid cell was assigned according to its global inertial coordinates. Specifically, the volume fraction is one for the cells located below the interface, and zero for the cells above. The same treatment of pressure function on the boundary condition also should be cleared. For the air field, the pressure is considered as constant, while the water pressure varies gradually depending on the depth of water.

2.3 Models and computational setup

The theory governing the vertical water entry of wedges and expressed by equations (4), (5) and (6) is validated for the case of oblique entry of a symmetric wedge first, mainly focusing on the vertical load characteristic. The oblique water entry has been chosen as the motion of the body resembles that of amphibious aircraft during landing and allows to study the effect of varying vertical velocity as well as variations of the horizontal velocity. In Russo et al. [23], the oblique impact of the wedge has been studied by systematically varying the velocity angle α, with the vertical and horizontal motions. The wedge has a width W=0.2 m and a deadrise angle β=37° and it is impacting with the symmetry axis oriented vertically, as seen in Figure 2a). The same model and condition are implemented in the numerical simulation. Besides, in order to carry out a relatively two-dimensional numerical simulation, the cell number in the y-direction is set to 1, and the cell size in the present study is 0.002 m. Figure 2b) shows the mesh topology and grid density with two zoom-in views. The length of the square boundary is 10 times the width of the wedge. The computational domain is discretized with structured quadrilateral grids and the minimum size of mesh is 0.0005 m. The right hand and bottom sides were set as velocity inlet, when the boundary condition of pressure outlet was specified on the top and the left sides (see Figure 2b)).

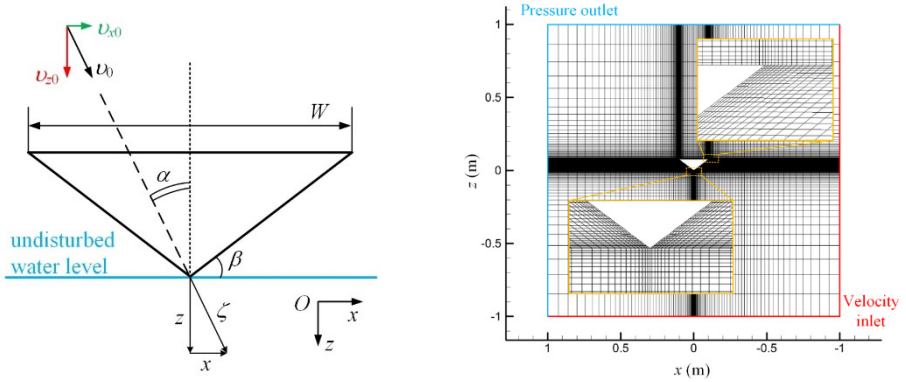

a) b)

Figure 2: Sketch of the wedge: a) geometric and dynamic parameters; b) grid topology and density of wedge.

Subsequently, the water landing of V-shaped hull on amphibious aircraft is studied to test the ability of the quantitative relations obtained from theoretical formulas for engineering application. A conventional configuration of the fuselage on amphibian is shown in Figure 3. The bottom of hull is separated into two parts, forebody and afterbody, by the step, making it easier to take off on water. The computational domain was created by a cuboid with size of $6\times2\times5L$ in length, width and height, respectively (see Figure 4), and is regarded large enough for the present study. The whole domain was comprised with Cartesian cells and prismatic boundary layer grids which surround the model and move together without deforming. Three tiers for refining meshes were assigned to the entire domain as follows: tier 3 for improving the accuracy of flow field solution near the hull; tier 2 and tier 1 fan-shaped regions to accommodate the large range of pitch motion. And the height of a cell in these tiers is $0.005L$, $0.01L$ and $0.015L$, respectively. The statistical result of grids in the whole domain is almost 12 million. Note that the wing and tail wing are taken into the consideration.

DOI: 10.13009/EUCASS2022-4541

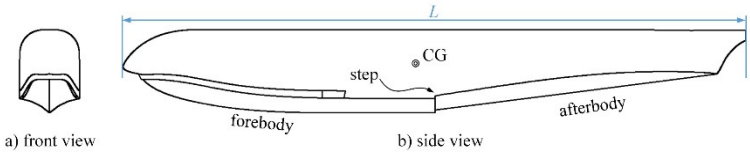

Figure 3: V-shaped hull configuration features of amphibious aircraft.

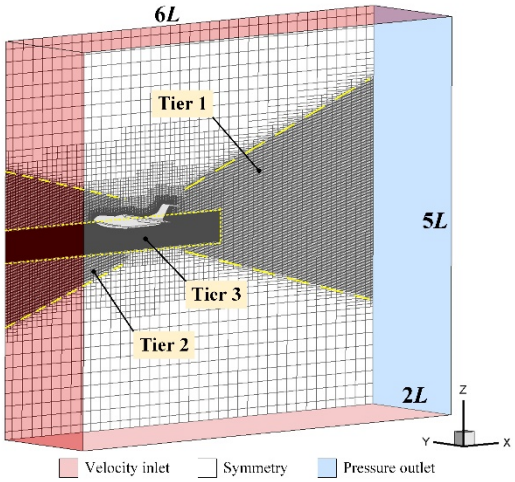

Figure 4: Computational domain and boundary conditions of the amphibious aircraft.

3. Results and Discussion

3.1 2D symmetric wedge

First, the accuracy and efficiency of the numerical method have been validated by a symmetric wedge. In the simulation, at t=0.001 s, the wedge is dropped against calm water from a small distance at 0.002m, entering the free surface with an initial resultant velocity 2.75 m/s and velocity angle $\alpha = 20°$. Figure 5 shows the comparison between present study and experimental data [23] in terms of the normalized resultant displacement ζ and acceleration $\ddot{\zeta}$. As can be seen, the results are in good agreement with experiments, though a little discrepancy occurs at the early stage of the acceleration. In fact, there should be a projection along the resultant velocity direction due to the gravity acceleration at the very first stage of the entry, while it is not easy for the measures carried out in the experiment to monitor. Overall, the solutions for the wedge are obtained which compares favorably with experimental data with satisfactory accuracy.

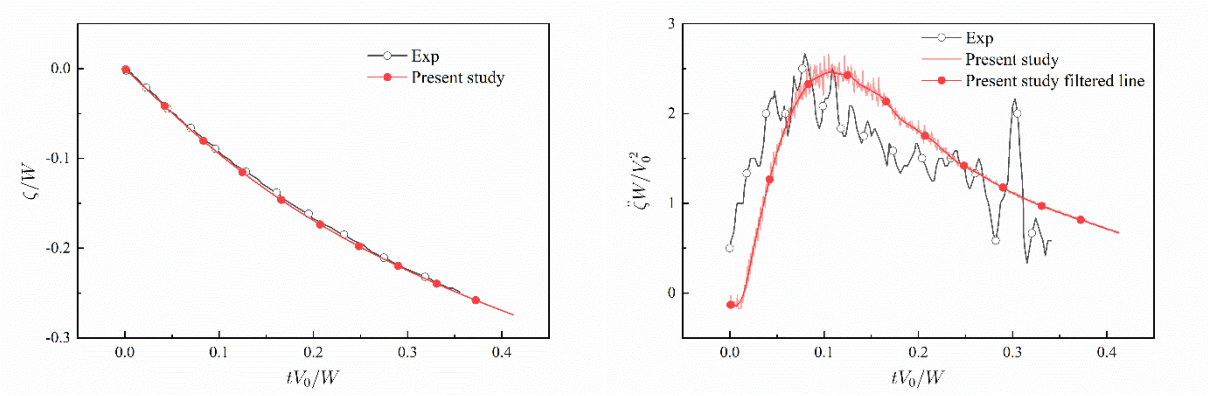

a) b)

Figure 5: Comparison of present study and experimental data: a) normalized resultant displacement; b) normalized resultant acceleration.

Subsequently, for understanding the effect of the variation of vertical velocity, the case of $\alpha = 20°$ is regarded as the reference case, where v_{x0} remains unchanged. Note that herein the initial resultant velocity is 3.132 m/s in the reference case. In comparison, α varies from 10° to 50° in 10° increments, implying a decrease of vertical velocity. The time histories of a_z, defined as $a_z = (F_w + F_a - Mg)/Mg$, are depicted in Figure 6a), along with several pink crosses

DOI: 10.13009/EUCASS2022-4541

marking the maximum value a_{zmax}. It indicates that constant υ_{x0} and systematically increasing α causes a significant reduction in a_z due to the corresponding decline in the υ_{z0}. Note that the positive values of a_z point to the opposite direction of gravity. Particularly, as υ_{z0} drops to a certain point, a_z will experience a moderating trend in proximity to zero, stating it 'smooth entry' [24]. The analysis of a_{zmax} and υ_{z0}, presented in Figure 6b), plots the solution of a_{zmax} as a linear function of υ_{z0}^2, supporting the relationship formulated in the Eq. (4), except the offset. Moreover, the other two series of simulations have been conducted by changing the constant value of υ_{x0}, together with the case of υ_{x0} equals zero, as depicted in Figure 7, where all data are identically on a straight line. Note that in the case of υ_{x0}=0.342 m/s, α varies from 5° to 50°. As evidenced in Table 1, we are cheerful to appreciate that the linear relation between a_{zmax} and υ_{z0}^2 exists, and only a small deviation could be observed in the slope k compared with the theoretical one derived from Eq. (4). However, there is an intercept value of b among the numerical results, maybe the gravity is responsible for the offset in the relation. On the other hand, it reveals the significant contribution of the vertical component of the velocity to the linear relation, regardless of the value of υ_{x0}.

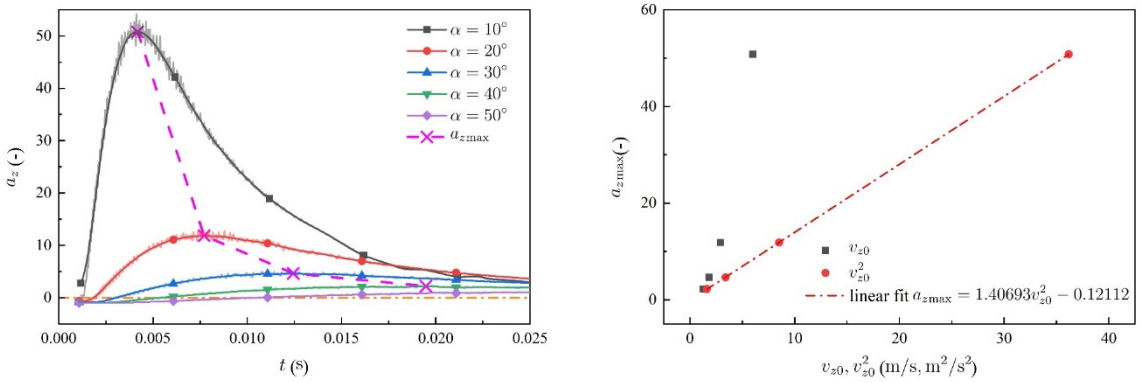

a) b)

Figure 6: Variation of acceleration z: a) versus time; b) versus initial vertical velocity.

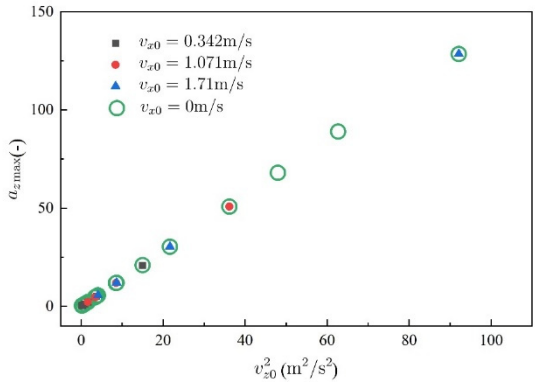

Figure 7: Effect of the horizontal velocity on the relation between a_{zmax} and υ_{z0}^2.

Table 1: Comparison of theoretical value and present study on wedge

	a_{zmax}			t^*, s			υ_z^*, m/s		
	k	err, %	b	k	err, %	b	k	err, %	b
Theoretical value	1.2807	-	-	0.0197	-	-	0.8333	-	-
υ_{x0} = 0.342 m/s	1.3588	6.09	-0.0509	0.0285	44.67	-0.0046	0.8010	-3.87	0.1121
υ_{x0} = 1.071 m/s	1.4069	9.85	-0.1211	0.0228	15.73	-0.0014	0.8367	0.41	0.0142
υ_{x0} = 1.710 m/s	1.3948	8.91	0.0364	0.0185	-6.09	-	0.8308	-0.30	0.0306

In Figure 8, we report the other four correlated variables, viz., time t^*, penetration depth z^*, velocity υ_z^* and the ratio of velocity κ, defined as $\kappa = \upsilon_z^* / \upsilon_{z0}$, for the four cases introduced earlier. In Eq. (6), a linear relation between t^* and reciprocal of initial vertical velocity $1/\upsilon_{z0}$ was established that is similar to the solution in Figure 8a), despite a small difference appears on k among the three cases. Comparing with the theoretical value listed in Table 1, the error, from 44.67% to -6.09%, shows an obvious decreasing with the growth of υ_{x0}. In fact, when reducing υ_{x0}, the initial vertical velocity becomes smaller, where gravity effect plays a more significant role causing the big error. In the illustration of

DOI: 10.13009/EUCASS2022-4541

z^* (see Figure 8b)), the values display a falling trend with the increase of υ_{x0}, where one can see that the greater the υ_{z0} is, z^* will get closer to a new asymptotic line slightly different from the theoretical result, however, z^* should remain unchanged in theory. Note that the theoretical solution was determined by M and β of the wedge, without υ_{z0}. Furthermore, the gray shaded area shows the range at which z^* is close to the constant value and the lowest value of υ_{z0} is almost 2.95 m/s in this model, implying that the theoretical solution is nearly valid only when certain condition on υ_{z0} is met. Figure 9 shows the water surface deformation around the wedge at t^* for different cases with a magenta region, where we can clearly observe the displacements of the apex remain almost the same as each other, despite different water jet zones form on the two sides. In the bottom-right figure, the spray seems to detach from the body and fall down. This is a consequence of the gravity. Besides, as shown in all contours, it indicates that $a_{z\max}$ appears before the wedge is completely submerged.

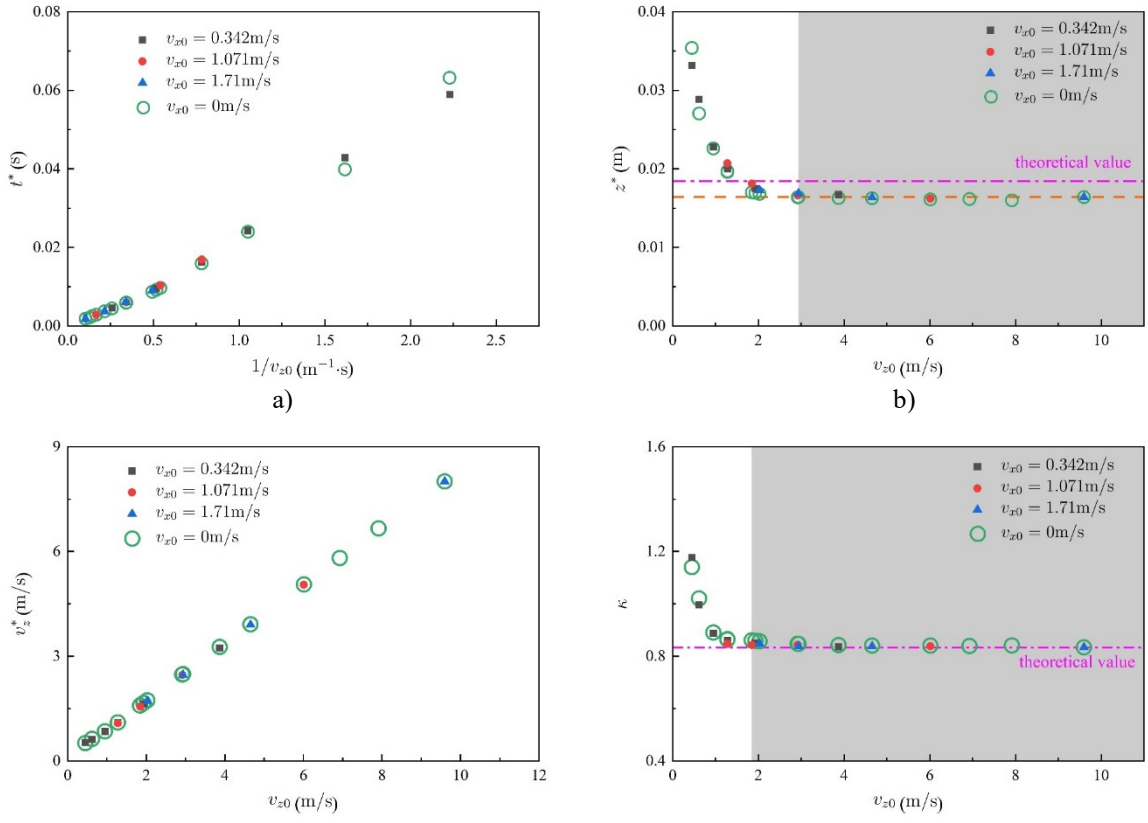

Figure 8: Effect of initial vertical velocity on variable dynamic parameters: a) t^*; b) z^*; c) υ_z^*; d) κ.

Moving to the relationship between υ_z^* and υ_{z0}, shown in Figure 8c) and Table 1, a slight difference among the simulations and theory on k can be observed, and the error value of k is almost below 5%. Furthermore, as shown in Figure 8d), the regularity is similar to the one obtained from z^*, and a gray shaded region also can be found where υ_z^* is 5/6 times υ_{z0}. In other words, the value 5/6 between υ_z^* and υ_{z0} can only be set up when υ_{z0} is greater than 1.85m/s, that is smaller than the limitation 2.95 m/s on z^*. As can be seen in Figure 6a), the acceleration experiences two phases, acceleration downwards and then upwards, before it reaches the highest point. Since the wedge, with a deadrise angle β =37°, performs a free fall motion, gravity plays a dominant role at the very early stage, leading to an accelerating period and an increase in the vertical velocity. Subsequently, with the increase of hydrodynamic force, the acceleration decreases in the downward direction and alternates to the upward direction gradually. Thus, it can be concluded from Figure 6a) that the smaller the initial vertical velocity is, the longer the accelerating time is, when a constant mass is assumed herein. Moreover, four distinctive points exceeding 1.0 are noticeable in Figure 8d), which means the vertical velocity of the body is larger than initial vertical velocity. Overall, it means that the accelerating phase not only lasts longer, but the effect of accelerating become more dominant than decelerating phase, as the initial vertical velocity decreases.

DOI: 10.13009/EUCASS2022-4541

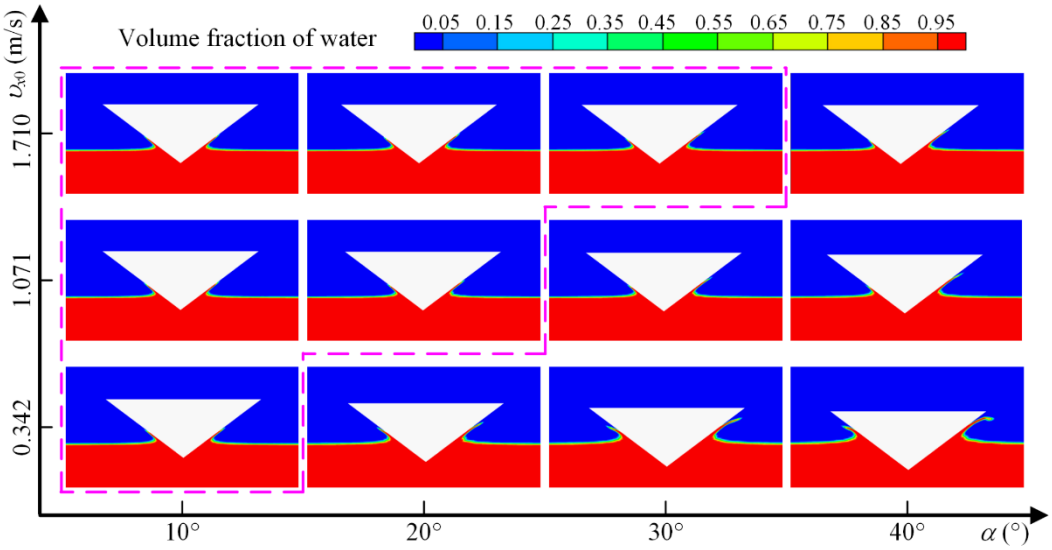

Figure 9: Snapshots of water surface deformation around the wedge at t^* with different υ_{x0} and α at the instant of maximum acceleration.

One thing that has to be highlighted is the momentum theorem (Eq. (1)) was obtained without gravity [18], while the gravitational field has been added into the numerical simulations. Nevertheless, the formulas (4), (5) and (6) derived from Eq. (1) are still available when the initial vertical velocity becomes larger. In other words, gravity can be neglected with larger velocities, and it has been evidenced in [13]. Moreover, with slow impact speeds, the gravity should be considered in the model [25], which can be used to explain the discrepancies occurred at the range of low velocities (see Figure 8b) and d)). Generally, based on the good collapse of the data from different initial horizontal velocity, it is believed that the initial vertical velocity plays a dominant role on the kinematic characteristics during wedge water entry with given shape parameters, indicating that the effect of initial horizontal velocity on the relations can be ignored. For all analytical solutions based on Eq. (4), (5) and (6) to keep them valuable, there is a threshold limit for the initial vertical velocity, contributing a good supplementary condition to the momentum theory. Besides, another thing that has to be emphasized specifically is the formula of the added mass, usually focusing on the vertical water entry, while it is found still available for the oblique entry.

3.2 Amphibious aircraft with V-shaped hull

Herein, the quantitative relations discussed above, (Eq. (4), (5) and (6)), are employed to examine the effect of initial vertical velocity υ_{z0} on the load characteristics of the V-shaped hull of the amphibious aircraft (see Figure 3). A set of numerical simulations is carried out with constant horizontal flight velocity υ_{x0}= 37 m/s, which is determined by the weight of aircraft G, wing area S and lift coefficient C_L regarding to the landing scenario, $\upsilon_{x0} = 0.94\sqrt{2G/\rho SC_L}$. The initial pitch θ_0 is set as 7° which is regarded as the suitable angle for landing event in the previous study [26]. Besides, the constraint of pitching angle θ is taken into account in present study, such as free pitch and stable pitch, considering the attitude control by pilots. Note that the wing components are taken into consideration in the present study.
Results, shown in Figure 10, indicate that a_z decreases when reducing υ_{z0} in both conditions. However, there is one thing in common, as υ_{z0} decreases, curves of a_z tend to convergence gradually, aside from the time lags. Figure 11 illustrates the pressure distribution at the bottom of the aircraft when a_z reaches its peak. The main fuselage portion striking with the free surface is the region over the forebody near the step. Note that the pressure coefficient displayed in the graph is defined as $C_p = (p - p_0)/(0.5\rho\upsilon_{x0}^2)$, where υ_{z0} is neglected being υ_{x0} = 37 m/s much greater than υ_{z0}.
The pressure peaks occur at the chine flare, after which the hydrodynamic pressure decreases with the formation of a triangular-shaped region of positive pressure near the step. Correspondingly, negative pressure areas occur behind the step and the stern of the fuselage. The occurrence of negative pressures at the back of the fuselage is a consequence of the longitudinal curvature and it can be easily explained by exploiting a 2D+t concept in which the local cross section undergoes a water exit phase [27]. The data also indicate that the high-pressure regions become smaller in size and reduce in magnitude when decreasing υ_{z0}, which is coherent with the overall downtrend on the evolutions of a_z revealed in Figure 10.

DOI: 10.13009/EUCASS2022-4541

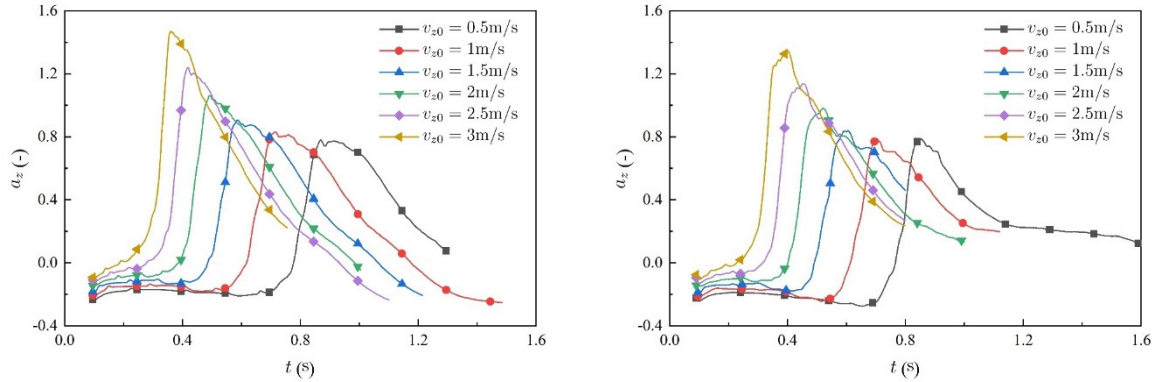

a) b)

Figure 10: Comparison of fixed and unfixed pitching condition on acceleration z with different initial vertical velocity: a) fixed; b) unfixed.

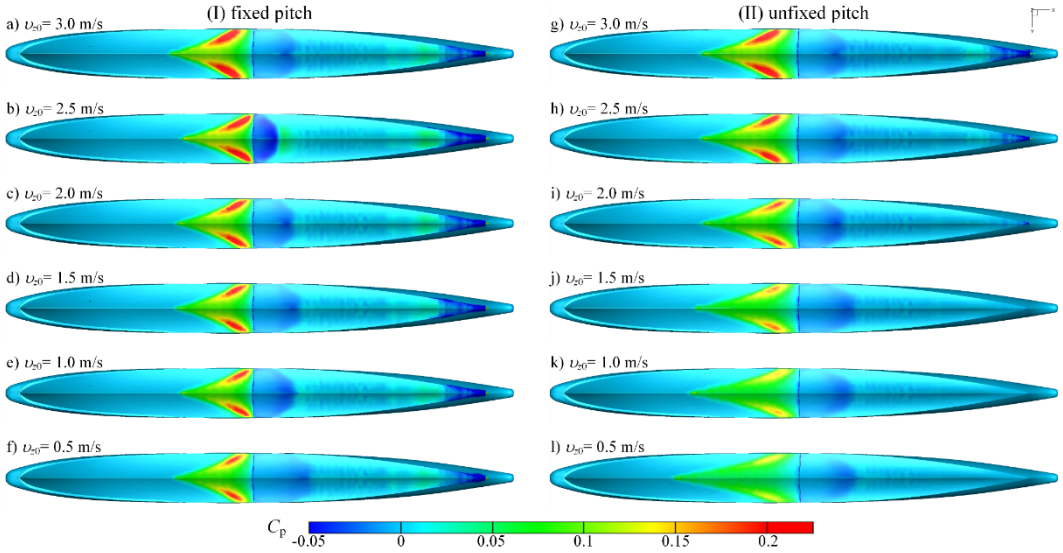

Figure 11: Pressure distribution at the bottom of the aircraft for different v_{z0} at t^*.

To obtain a better comprehension of the effect of impact velocity on accelerations, the maximal values of a_z are gathered and reported with the square of vertical velocity v_{z0}^2 in Figure 12. Unfortunately, the theoretical estimation about the slope k on $a_{z\max}$-v_{z0}^2 doesn't hold in this case. In the presence of a high horizontal speed, the pressure doesn't depend much on vertical velocity but rather on horizontal velocity, pitch angle and pitch dynamics. Furthermore, there are the effects associated with the suction and a double-stepped planing phenomenon which are not accounted for in the theoretical model (see Figure 13). Whereas, the linearity on $a_{z\max}$-v_{z0}^2 can be formed as well, despite a little deviation appears when v_{z0} is lower than 1m/s on the fixed pitching situation. The most results of $a_{z\max}$ with constant pitch is above that with free pitch. For instance, the high-pressure region presented in Figure 11c) is larger than that in Figure 11i). In all cases, what we can conclude is to evaluate the variation of acceleration about an amphibious aircraft on water landing which has V-shaped cross-section, a linear relation can be predicted through a small dataset of v_{z0}, at least four results.

DOI: 10.13009/EUCASS2022-4541

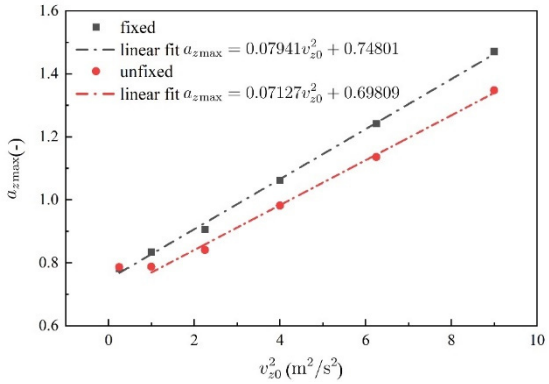

Figure 12: Effect of the pitching on the relation between $a_{z\max}$ and υ_{z0}^2.

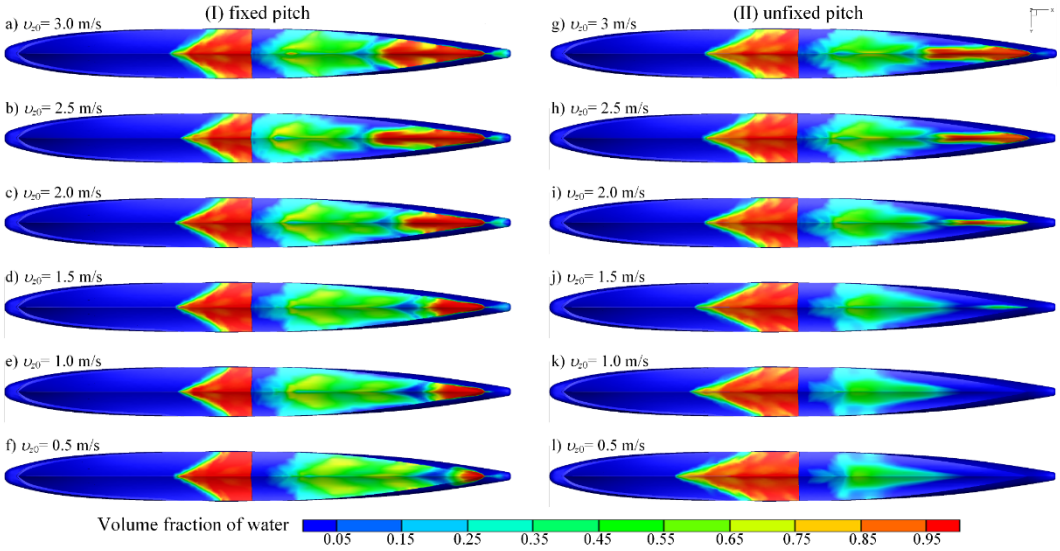

Figure 13: Water volume fraction at the bottom of the aircraft for different υ_{z0} at t^*.

Since a considerable change on the estimation about $a_{z\max}$-υ_{z0}^2, it is necessary to check the effectiveness on Eq. (5) and (6). Figure 14 shows the variation of other four factors with the change of υ_{z0}, when the acceleration reaches its peak. As it can be seen in Figure 14a), the larger the vertical velocity is, the shorter the time interval is, implying that the load distribution in time is smoother for lowerυ_{z0}. Moreover, there is no proportionality between t^* and $1/\upsilon_{z0}$ in both cases of fixed and free pitch. Moving to penetration depth z^* Figure 14b), a quite different evolution emerges between the fixed and free pitch condition. Results of the case of fixed pitch exhibit small variations about the mean value, whereas, in the case of free pitch z^* increases as υ_{z0} increases and it approaches a constant value gradually. It is also worth noticing that there is an inverse trend compared to the cases of wedge and cabin section. The motion, z^*, seems more constant when an attitude control mode (fixed pitch) exerting on the aircraft.

The results of maximal draught $z_{\max}$, reached by the hull, are also depicted in Figure 14b). It can be seen obviously that $z_{\max}$ is above z^*, implying that while a_z attains its maximum, the aircraft continues to move downwards. It shows a monotonous increasing trend on the function of $z_{\max}$ to υ_{z0} for the case of fixed pitch, while a valley occurs at the curve for unfixed pitch. Turning to the behavior of the corresponding velocity υ_z^*, it is interesting to see that the two cases share the same evolution in υ_z^*-υ_{z0} generally, as presented in Figure 14c) and d). Specifically, there is a turning point where υ_{z0} equals 1.5 m/s, whereas the trend is similar afterwards. On the left side of turning point, the results of fixed pitch are lower than that of free pitch. The blue dashed rectangle indicates the range at which υ_z^* is above υ_{z0}, in other words, $\kappa > 1$, implying that the gravity of the body plays a significant role when υ_{z0} is smaller than a constant value. It is more clearly to identify that, two stages, concerning acceleration and deceleration phase, exist indeed before the overload reaches its maximum with varying initial vertical velocity. However, as long as the initial impact velocity is smaller than a constant value, the effect of deceleration is not evident enough, thus making the ratio of the corresponding velocity vs the initial velocity greater than one. It is not easy to find a relation for υ_z^*-υ_{z0} which is not desirable as we expected. However, it should be noted all data amazingly approach the theoretical solution of $\kappa = 5/6$, which means κ is still available to some extent. Therefore, the regulation derived from Eq. (4) and Eq. (5) are partly useful for the development tendency prediction on $a_{z\max}$ and κ through a simple analysis.

DOI: 10.13009/EUCASS2022-4541

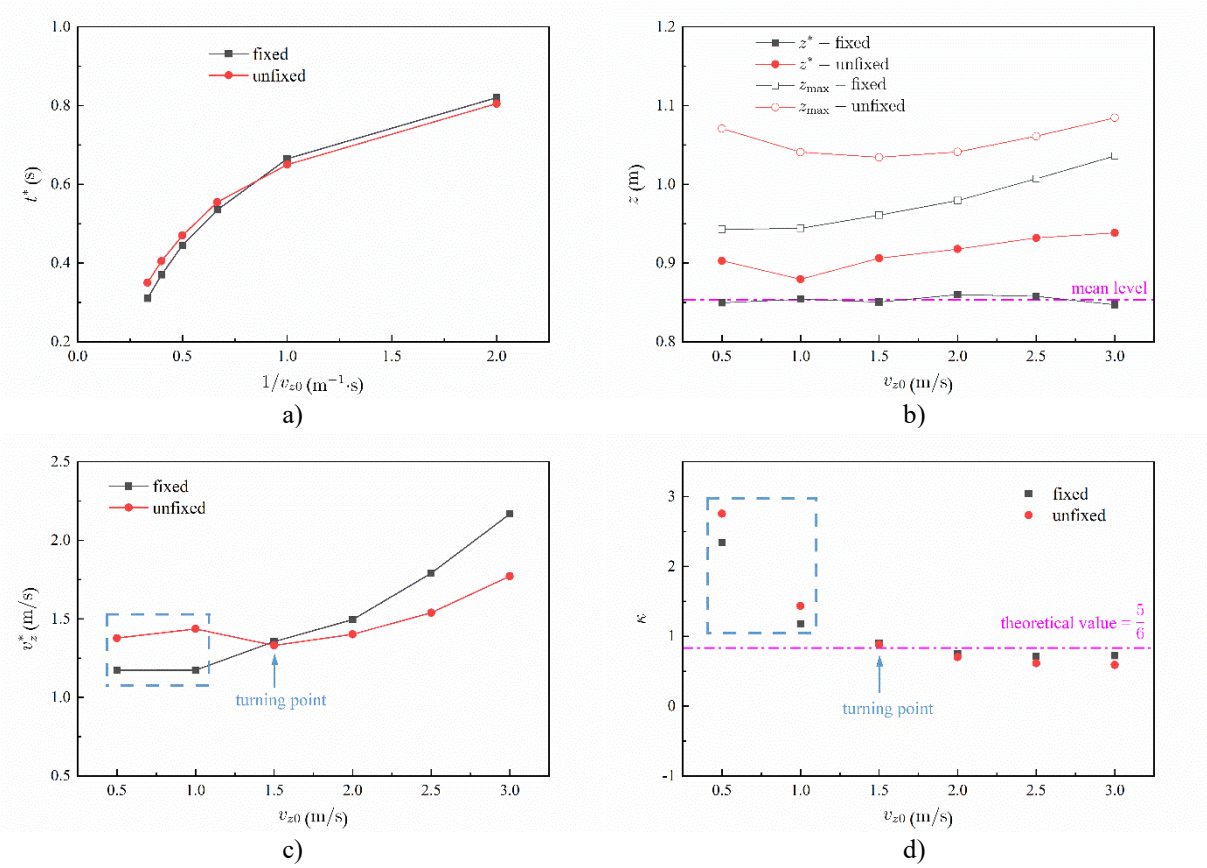

Figure 14: Effect of initial vertical velocity on variable dynamic parameters: a) t^*; b) z^*; c) v_z^*; d) κ.

4. Conclusion

In the present study, the load characteristics of three models, such as a 2D symmetric wedge water entry and an amphibious aircraft landing on water have been investigated numerically. The effect of initial vertical velocity on the maximum acceleration, together with several relationships based the transformation of momentum theorem, have been thoroughly analysed. Contributions and findings are summarized, which can be described as:

1) For the V-shaped sectional area of body impacting on water surface, the maximum vertical acceleration increases with the initial vertical velocity, and it is found herein that the value of maximal acceleration is proportional to the square of the initial velocity, although large differences in the slope occur in the case of stepped hull.

2) Another significant parameter, that the two models have the same regularity, is the ratio of the corresponding velocity to the initial velocity, κ. Following the theoretical formulation, the value should be constant, 5/6, while the numerical results approach to it in the case of large initial vertical velocity. It indicates that a threshold value of initial vertical velocity needs to be emphasized to make the theoretical result available. In other words, gravity can be neglected with larger velocities, however, with slow impact speeds, the gravity should be considered in the model.

3) For the relationship between penetration depth and the initial vertical velocity, the theoretical value can be treated as the asymptotic line with the increase of velocity in the 2D wedge case. Considering the complicated geometry of the hull, it is hard to determine the theoretical estimation. The numerical results of fixed pitch present a constant situation, whereas a constant value is not reached in the case of free pitch.

4) Looking into other two linear relations, they can be established upon the wedge compared with the theoretical results, while it is invalid for the hull.

Acknowledgements

This work has been supported by China Scholarship Council (CSC, No. 202106830092) and the Project TORPEDO (inTerazione fluidO stRuttura in ProblEmi Di impattO) cooperated in the Institute of Marine Engineering of the National Research Council of Italy.

DOI: 10.13009/EUCASS2022-4541

References

[1] Qiu, L., and Song, W. 2013. Efficient decoupled hydrodynamic and aerodynamic analysis of amphibious aircraft water takeoff process. *Journal of Aircraft*. 50(5): 1369-1379.

[2] Hughes, K., Vignjevic, R., Campbell, J., Vuyst, T. D., Djordjevic, N., and Papagiannis, L. 2013. From aerospace to offshore: bridging the numerical simulation gaps-simulation advancements for fluid structure interaction problems. *International Journal of Impact Engineering*. 61: 48-63.

[3] Neuberg and Drimer, N. 2017. Fatigue limit state design of fast boats. *Marine Structures*. 55: 17-36.

[4] Siemann, M. H., Schwinn, D. B., Scherer, J., and Kohlgruber, D. 2017. Advances in numerical ditching simulation of flexible aircraft models. *International Journal of Crashworthiness*. 23(2): 236-251.

[5] Von Karman, T. 1929. The impact on seaplane floats during landing. NACA TN-321.

[6] Wagner, H. 1932. Phenomena associated with impacts and sliding on liquid surface. *Journal of Applied Mathematics and Mechanics*. 12(4): 193-215. (in German)

[7] Zhao, R., and Faltinsen, O. M. 1993. Water entry of two-dimensional bodies. *Journal of Fluid Mechanics*. 246: 593-612.

[8] Scolan, Y. M., and Korobkin, A. A. 2001. Three-dimensional theory of water impact. Part 1. inverse wagner problem. *Journal of Fluid Mechanics*. 440: 293-326.

[9] Korobkin, A. 2004. Analytical models of water impact. *European Journal of Applied Mathematics*. 15(6): 821-838.

[10] Korobkin, A. A., and Scolan, Y. M. 2006. Three-dimensional theory of water impact. Part 2. linearized wagner problem. *Journal of Fluid Mechanics*. 549: 343-373.

[11] Wu, G. X., and Sun, S. L. 2014. Similarity solution for oblique water entry of an expanding paraboloid. *Journal of Fluid Mechanics*. 745: 398-408.

[12] Breton, T., Tassin, A., and Jacques, N. 2020. Experimental investigation of the water entry and/or exit of axisymmetric bodies. *Journal of Fluid Mechanics*. 901: A37.

[13] Zekri, H. J., Korobkin, A. A., and Cooker, M. J. 2021. Gravity effect on water entry during an early stage. *Journal of Fluid Mechanics*. 916: A10.

[14] Wang, J., Lugni, C., and Faltinsen, O. M. 2015. Experimental and numerical investigation of a freefall wedge vertically entering the water surface. *Applied Ocean Research*. 51: 181-203.

[15] Gong, K., Liu, H., and Wang, B. 2009. Water entry of a wedge based on sph model with an improved boundary treatment. *Journal of Hydrodynamics*. 21(6): 750-757.

[16] Abraham, J., Gorman, J., Reseghetti, F., Sparrow, E., Stark, J., and Shepard, T. 2014. Modeling and numerical simulation of the forces acting on a sphere during early-water entry. *Ocean Engineering*. 76: 1-9.

[17] Yu, P., Shen, C., Zhen, C., Tang, H., and Wang, T. 2019. Parametric study on the free-fall water entry of a sphere by using the RANS method. *Journal of Marine Science and Engineering*. 7(5): 122.

[18] Mei, X., Liu, Y., and Yue, D. K. P. 1999. On the water impact of general two-dimensional sections. *Applied Ocean Research*. 21: 1-15.

[19] Panciroli, R., Abrate, S., and Minak, G. 2013. Dynamic response of flexible wedges entering the water. *Composite Structures*. 99: 163-171.

[20] Iafrati, A., Carcaterra, A., Ciappi, E., and Campana, E. F. 2000. Hydroelastic analysis of a simple oscillator impacting the free surface. *Journal of Ship Research*. 44(4): 278-289.

[21] Hirt, C. W., and Nichols, B. D. 1981. Volume of fluid (VOF) method for the dynamics of free boundaries. *Journal of Computational Physics*. 39(1): 201-225.

[22] Xiao, T., Lu, Y., Deng, S., Zhi, H., Zhu, Z., and Chen, J. 2021. Hydrodynamic characteristics of a helicopter ditching on different positions of wavy water. *Journal of Aircraft*. 58(5): 1-12.

[23] Russo, S., Jalalisendi, M., Falcucci, G., and Porfiri, M. 2018. Experimental characterization of oblique and asymmetric water entry. *Experimental Thermal and Fluid Science*. 92: 141-161.

[24] Vincent, L., Xiao, T., Yohann, D., Jung, S., and Kanso, E. 2018. Dynamics of water entry. *Journal of Fluid Mechanics*. 846: 508-535.

[25] Bertram, V. 2012. Practical Ship Hydrodynamics, 2nd ed. Butterworth-Heinemann, Kidlington.

[26] Lu, Y., Xiao, T., Deng, S., Zhi, H., Zhu, Z., and Lu, Z. 2021. Effects of initial conditions on landing performance of the amphibious aircraft. *Acta Aeronautica et Astronautica Sinica*. 42(7): 159-170. (in Chinese)

[27] Del Buono, A., Bernardini, G., Tassin, A., and Iafrati, A. 2021. Water entry and exit of 2d and axisymmetric bodies. *Journal of Fluids and Structures*. 103: 103269.